



HAL
open science

Influence of the water content on the complex conductivity of bentonite

Jad El Alam, André Revil, Pierre Dick

► **To cite this version:**

Jad El Alam, André Revil, Pierre Dick. Influence of the water content on the complex conductivity of bentonite. *Engineering Geology*, 2023, 322, pp.107183. 10.1016/j.enggeo.2023.107183 . irsn-04200615

HAL Id: irsn-04200615

<https://irsn.hal.science/irsn-04200615>

Submitted on 31 Oct 2023

HAL is a multi-disciplinary open access archive for the deposit and dissemination of scientific research documents, whether they are published or not. The documents may come from teaching and research institutions in France or abroad, or from public or private research centers.

L'archive ouverte pluridisciplinaire **HAL**, est destinée au dépôt et à la diffusion de documents scientifiques de niveau recherche, publiés ou non, émanant des établissements d'enseignement et de recherche français ou étrangers, des laboratoires publics ou privés.



Distributed under a Creative Commons Attribution - NonCommercial - NoDerivatives 4.0 International License

24 **Abstract.** Compacted bentonite is considered as a potential buffer material for deep geological
25 disposals of high-level nuclear wastes. Methodologies to non-intrusively monitor the water
26 content of such materials are important in the context of the safety of these storage facilities
27 and for various engineering applications as well. Induced polarization is a non-intrusive
28 geophysical method sensitive to the water content of porous media. We investigated the
29 complex conductivity spectra of 69 samples made of 2 distinct MX80 bentonites, one in the
30 form of powder from crushed pellets (Type I) and the other in the form of a granulated bentonite
31 mixture (GBM, type II). The samples are prepared at different compaction states and
32 saturations. The pore water conductivity of the core samples is estimated to be $\sim 2.5 \text{ S m}^{-1}$
33 (25°C) by two different methods. The complex conductivity spectra were obtained at room
34 temperature ($25 \pm 2^\circ\text{C}$) in the frequency range 1 Hz-45 kHz. In-phase and quadrature
35 conductivities reflect conduction and polarization processes, respectively. At a given frequency,
36 both the in-phase and quadrature conductivities increase with the water content along a trend
37 that is independent of the compaction state. An induced polarization model based on the
38 dynamic Stern layer model is used to explain these results. The first Archie's exponent is
39 inferred from the formation factor using the in-phase conductivity data versus the pore water
40 conductivity data at different salinities (NaCl, 25°C). The dynamic Stern layer model correctly
41 predicts the dependence of the in-phase conductivity, quadrature conductivity, and normalized
42 chargeability with the water content and Cation Exchange Capacity (CEC). This petrophysical
43 work can easily be applied to time-domain induced polarization data in field conditions.

44

45 **Key words:** Induced polarization; bentonite, water content; hydrogeophysics.

46

47 **1. Introduction**

48
49 Isolating high-level long-lived radioactive wastes from the biosphere is a priority across
50 the world to avoid any significant release of radionuclides that may be dangerous to humankind
51 (Madsen, 1998; Volckaert et al., 2004). In this context, Deep Geological Repositories (DGR)
52 are foreseen to contain radioactive wastes in a tight and stable geological formation at depths
53 of several hundred of meters. DGRs are designed to be passively safe and not reliant on active
54 safety systems that would necessitate support from future generations. The post-closure passive
55 safety principally relies on specifically designed engineered barriers (e.g., waste packages and
56 engineered backfill materials) and host rock properties that will inhibit and reduce the
57 migration of radioactive wastes (Madsen, 1998; Volckaert et al., 2004; Okko and Rautjaervi,
58 2006; Pettersson and Loennerberg, 2008; Köhler et al., 2015; Norris, 2017).

59 In the concept of DGRs of high-level radioactive waste (HLW), a multi-barrier system
60 is usually adopted. It includes bentonite and retaining structures with concrete (e.g. mechanical
61 plug or structure liner in tunnels and shafts). Bentonite-based Engineered Barrier Systems
62 (EBS) are generally envisioned as a potential solution for the repository design because of their
63 low permeability, large swelling capacity and high retention properties, as well as thermal
64 stability among other wanted characteristics (Kanno and Wakamatsu, 1992; Chapman 2006;
65 Chen et al., 2014).

66 One of the options for the repository design is to place the bentonite in the form of high-
67 density compacted blocks in the vicinity of waste canisters to effectively seal preferential
68 pathways for the migration of fluids (Mokni et al., 2016; Norris, 2017; Guo and Fall, 2021).
69 The initially unsaturated bentonite is expected to sorb the surrounding fluids and compounds
70 to retard their migration to the biosphere. Its high swelling capacity should impose sufficient
71 swelling pressure to ensure a good sealing performance (generally a large swelling pressure
72 results in low permeability). At the opposite, the concrete will undergo some chemical effects

73 from groundwater and will thus degrade over time, generating a high-pH alkaline solution that
74 will migrate into the compacted bentonite and alter its hydro-mechanical behaviour and
75 possibly jeopardize the safety of the repository.

76 Though the relationship between compaction (commonly described by the dry density
77 of the compacted bentonite) and the swelling pressure has been widely studied (e.g., Gens and
78 Alonso, 1992, Studds et al. (1998); Cui et al., 2002; Komine, 2004), recent experimental results
79 show that the swelling pressure increases exponentially as the dry density of compacted
80 bentonite increases (Villar and Lloret, 2008; Schanz and Al-Badran, 2014). It also decreases as
81 the salinity of the pore water solution increases (Alawaji, 1999; Suzuki et al., 2005; Karnland
82 et al., 2007; Herbert et al., 2008; Komine et al., 2009; Chen et al., 2015; Sun et al., 2015).
83 However, for densely compacted bentonites with a high pore fluid salinity, the swelling
84 pressure decreases less significantly as the salt concentration increases (Karnland et al., 2005;
85 Castellanos et al., 2008; Siddiqua et al., 2011; Zhu et al., 2013). Hence, understanding and
86 being able to monitor and predict the swelling characteristics of bentonite through time, with
87 regards to changing porewater chemistry, is essential to guarantee the long-term safety of
88 DGRs.

89 In this framework, monitoring the porewater evolution (content and chemistry), and
90 linking it to the bentonite's petrophysical parameters (CEC, specific surface, saturation,
91 porosity, density, etc.) through time and space appears essential to assess and predict the long-
92 term performance of an EBS. However, in a DGR, the direct monitoring of the EBS with wired
93 sensors will probably not be achieved in the buffer as wires can provide a preferential pathway
94 for water and thus for radionuclide leakage (White et al. 2017). Geophysics, particularly
95 geoelectrical methods, is potentially an ideal way to overcome this problem as: (i) it can be
96 designed in a non-intrusive manner; (ii) it is sensitive to variations in water and clay content;
97 (iii) it allows dynamic phenomena to be monitored over time; and (iv) it allows local anomalies

98 to be captured that isolated sensors cannot detect. Among the electrical methods available,
99 spectral induced polarisation (SIP) appears to be the most suitable method, as it is not only
100 sensitive to variations in water content but also to the mineralogical and chemical variability
101 of the water and is therefore very convenient to monitor the EBS (Cosenza et al. 2007; Hermans
102 et al. 2015; Merritt et al. 2016; López-Sánchez et al. 2017; Wang et al. 2017).

103 Induced polarization is a non-intrusive method currently playing a key role in the realms
104 of hydrogeophysics (Kemna et al., 2012; Ntarlagiannis et al., 2019) and biogeophysics (Martin,
105 2012; Revil et al., 2012; Martin et al., 2015). It has a long history in geophysics for which it
106 was primary used for a long time for ore detection (Seigel, 2007). Induced polarization
107 properties are sensitive to the water content of porous rocks and sediments (Börner, 1992;
108 Schön, 1996). It is a low-frequency active technique looking not only at imaging electrical
109 conductivity but also in the ability of porous media to store reversibly electrical charges when
110 submitted to an electrical current (Vinegar and Waxman, 1984). In the absence of metallic
111 particles, the storage of these charges is done through the polarization of the electrical double
112 layer coating the surface of the grains (Dukhin and Shilov, 1974; Dias, 2000; Revil, 2013a, b).
113 The relevant property is called normalized chargeability in time-domain induced polarization
114 or quadrature conductivity in frequency-domain induced polarization. Both are proportional to
115 each other.

116 In frequency-domain induced polarization, complex conductivity spectra are obtained
117 in a broad low frequency-range, typically 1 mHz to 100 kHz, by looking at the amplitude of
118 the conductance and the phase lag between the current and the electrical field. Previous studies
119 have been undertaken to better understand the induced polarization response of clayey
120 materials including shaly sands and sandstones (e.g., Vinegar and Waxman, 1984; Revil et al.,
121 2013b), soils (Revil et al., 2017), clay-sand mixtures (Breede et al., 2012), source shales and
122 mudrocks (Revil et al., 2013a), and argillites and clay-rocks (Kruschwitz and Yaramanci, 2004;

123 Comparon, 2005; Ghorbani et al., 2009; Jougnot et al., 2010a, b; Okay et al., 2013, 2014; Tartrat
 124 et al., 2019). In addition, induced polarization properties can be influenced by the presence of
 125 metallic ions in the pore water (Vaudelet et al., 2011) and pyrite present in black shales and
 126 some mudrocks (Tartrat et al., 2019).

127 To the best of our knowledge, bentonite powders subjected to changes in saturation and
 128 compaction state have never been evaluated with induced polarization so far. In this study, we
 129 investigate the complex conductivity spectra of 69 core samples at different water contents
 130 corresponding to different saturation rates and compaction states. Our goals of this study are
 131 (1) to establish a database for the complex conductivity spectra of bentonite at different
 132 compaction states and volumetric water contents. Saturations range from 35% to 100%,
 133 volumetric water contents range between 16 % to 71%. (2) Our second goal is to explain the
 134 observed trends found between complex conductivity spectra and saturation and compaction
 135 states using the dynamic Stern layer model of induced polarization developed (see Revil, 2012;
 136 2013). (3) Our final goal is to assess the suitability of the SIP method to monitor the spatial and
 137 temporal petrophysical heterogeneities of bentonite seals in geological disposals.

138

139 **2. Theory**

140 Induced Polarization (or complex conductivity) is a geophysical technique that involves
 141 measuring the low-frequency response (<100 kHz) of a medium under the influence of an
 142 applied alternating electrical field (Olhoeft, 1981; Börner, 1992). Measurements can also be
 143 performed in either time-domain or frequency-domain (Kemna et al., 2012). When a harmonic
 144 electric field $\mathbf{E} = \mathbf{E}_0 \exp(+i\omega t)$ (t refers to time) is applied, the complex conductivity σ^* is
 145 characterized by its amplitude $|\sigma|$ (in S m^{-1}) and phase lag φ (in rad), which are both measured
 146 using an impedance meter. We can define a complex conductivity as,

$$147 \quad \sigma^*(\omega) = |\sigma|e^{i\varphi} = \sigma'(\omega) + i\sigma''(\omega), \quad (1)$$

148 where $\omega = 2 \pi f$ denotes the pulsation frequency, f the frequency (Hertz), i is the pure
 149 imaginary number, and σ' and σ'' denote the real (in-phase) and imaginary (quadrature or out-
 150 of-phase) conductivity, respectively. Since the in-phase conductivity is the conductivity in
 151 absence of polarization (zero phase), it refers to the process of pure conduction (i.e., charge
 152 electromigration) while the quadrature conductivity refers to the mechanism of pure reversible
 153 charge storage, both under the action of an applied electrical field. Thus, such a decomposition
 154 is useful in terms of the underlying physics instead of dealing with amplitude and phase of the
 155 impedance.

156 In order to further understand induced polarization, we need to scale our analysis to the
 157 particle size. The polarization of a clay particle (smectite in the case of bentonite) is associated
 158 with the polarization of the electrical double layer coating the surface of the grains (Figure 1).
 159 This double layer comprises an inner layer called the Stern layer and an outer layer called the
 160 Gouy-Chapman layer.

161 The in-phase conductivity depends on two contributions corresponding to the bulk and
 162 surface conductivities. The bulk conductivity refers to conduction in the water phase located in
 163 the pore space while the surface conductivity is characterized by conduction in the electrical
 164 double layer coating the surface of the grains. At a given frequency, the in-phase conductivity
 165 can be expressed in the high salinity asymptotic limit by (see Revil et al., 2021, and references
 166 therein):

$$167 \quad \sigma'(\omega) = \theta^m \sigma_w + \sigma_s(s_w, \omega), \quad (2)$$

168 where σ_w (S m^{-1}) denotes the pore solution conductivity, $\theta = s_w \phi$, θ denotes the dimensionless
 169 volumetric water content (s_w is the saturation and ϕ is the connected porosity, both
 170 dimensionless), and the exponent m (dimensionless) is called the first Archie exponent, the
 171 cementation exponent, or the porosity exponent. The formation factor F (dimensionless) is
 172 connected to porosity by $F = \phi^m$ (Archie's law, Archie, 1942). Only in absence of surface

173 conduction in the electrical double layer coating the surface of the minerals and at saturation,
 174 the formation factor is given as the ratio of the resistivity of the porous material divided by the
 175 resistivity of the pore water. The quantity σ_s ($S m^{-1}$) denotes the surface conductivity associated
 176 with conduction in the electrical double layer. Since there is a lot of confusion in the literature
 177 regarding Archie's law, it is good to recall that Archie's law is not a conductivity equation and
 178 is valid whatever the strength of surface conductivity with respect to bulk conductivity
 179 associated with the pore water conductivity.

180 In order to interpret complex conductivity spectra in a partially-saturated and metal-
 181 free porous material, a model called the dynamic Stern layer model is required (e.g., Revil,
 182 2013a, b, Revil et al., 2017). In the framework of this model, the complex conductivity is
 183 written as (Revil et al., 2017a)

$$184 \quad \sigma^*(\omega) = \sigma_\infty - M_n \int_0^\infty \frac{h(\tau)}{1 + (i\omega\tau)^{1/2}} d\tau, \quad (3)$$

185 where τ is a relaxation time (in s) and $h(\tau)$ denotes a (normalized) probability density for the
 186 relaxation times of the material. The real-valued quantity σ_∞ ($S m^{-1}$) corresponds to the
 187 instantaneous conductivity of the soil while the real-valued term σ_0 ($S m^{-1}$) corresponds to its
 188 DC (Direct Current) conductivity (Figure 1). Their expressions are further described below in
 189 terms of textural properties and environmental conditions. The normalized chargeability M_n
 190 corresponds to the difference between the instantaneous conductivity and the DC conductivity
 191 $M_n \equiv \sigma_\infty - \sigma_0$. Note that if the normalized chargeability is determined between two
 192 intermediate frequencies f_1 and f_2 (i.e., $M_n(f_1, f_2) = \sigma'(f_2) - \sigma'(f_1), f_2 > f_1$), it is necessarily smaller
 193 than the integrated normalized chargeability $M_n \equiv \sigma_\infty - \sigma_0$ because the conductivity
 194 monotonically increases with the frequency.

195 The instantaneous and DC conductivities as well as the normalized chargeability of
 196 bentonite are given by

$$197 \quad \sigma_{\infty} = \phi^m s_w^n \sigma_w + \phi^{m-1} s_w^{n-1} \rho_g B \text{CEC}, \quad (4)$$

$$198 \quad \sigma_0 = \phi^m s_w^n \sigma_w + \phi^{m-1} s_w^{n-1} \rho_g (B - \lambda) \text{CEC}, \quad (5)$$

$$199 \quad M_n = \phi^{m-1} s_w^{n-1} \rho_g \lambda \text{CEC}, \quad (6)$$

200

201 where equation (6) results from equations (4) and (5), ρ_g denotes the grain density (2770 kg
 202 m^{-3} for smectite), and CEC denotes the cation exchange capacity of the soil expressed in C kg^{-1}
 203 ¹ or in $\text{meq}/100 \text{ g}$ ($1 \text{ meq}/100 \text{ g} = 963.20 \text{ C kg}^{-1}$ in SI units), B (in $\text{m}^2 \text{s}^{-1} \text{V}^{-1}$) denotes the apparent
 204 mobility of the counterions for surface conduction (associated with the in-phase conductivity)
 205 and λ (in $\text{m}^2 \text{s}^{-1} \text{V}^{-1}$) denotes the apparent mobility of the counterions for the polarization
 206 associated with the quadrature conductivity (see Vinegar and Waxman, 1984). We have $B(\text{Na}^+$,
 207 $25^\circ\text{C}) = 3.1 \pm 0.3 \times 10^{-9} \text{ m}^2 \text{s}^{-1} \text{V}^{-1}$ and $\lambda(\text{Na}^+, 25^\circ\text{C}) = 3.0 \pm 0.7 \times 10^{-10} \text{ m}^2 \text{s}^{-1} \text{V}^{-1}$. A dimensionless
 208 number R was introduced by Revil et al. (2017) as $R = \lambda / B \approx 0.10 \pm 0.02$. The two mobilities
 209 are considered to be independent of the salinity.

210 When a clayey material is partially saturated with a pore water electrolyte and assuming
 211 that $m \approx n$, Revil (2013a, b) and Revil et al. (2021) obtained the following relationships from
 212 equations (4) to (6):

$$213 \quad \sigma_{\infty} = \theta^m \sigma_w + \theta^p \rho_g B \text{CEC}, \quad (7)$$

$$214 \quad \sigma_0 = \theta^m \sigma_w + \theta^p \rho_g (B - \lambda) \text{CEC}, \quad (8)$$

$$215 \quad M_n = \theta^p \rho_g \lambda \text{CEC}. \quad (9)$$

216

217 The case of the presence of metallic particles (like pyrite and magnetite) is discussed by Misra
 218 et al. (2016) but our bentonite core samples are free of such semi-conductors from X-Ray
 219 Diffraction (XRD) analysis.

220 Considering the quadrature conductivity at the geometric mean frequency of two
 221 frequencies f_1 and f_2 and the normalized chargeability defined as the difference between the in-
 222 phase conductivity at the frequency $f_2 (> f_1)$ and the in-phase conductivity at the lower

223 frequency f_1 , we can connect the quadrature conductivity and the normalized chargeability with
 224 (Van Voorhis et al., 1973; Revil et al., 2017)

$$225 \quad \sigma''(\sqrt{f_1 f_2}) \approx -\frac{M_n(f_1, f_2)}{\alpha}, \quad (10)$$

$$226 \quad \alpha \approx \frac{2}{\pi} \ln A, \quad (11)$$

227
 228 and A denotes the number of decades between f_1 and f_2 (for 3 decades, we have $A = 10^3$ and
 229 $\alpha \approx 4.4$). Equations (6) and (7) provide the relationship between the quadrature conductivity
 230 and the CEC. Equations (7) and (8) are not related to the dynamic Stern layer model and can
 231 be derived from the constant phase model. That said, as noticed in Revil et al. (2017a), they are
 232 very accurate for soils characterized by broad distribution of the relaxation times. From
 233 equation (7) and the expression of the surface conductivity, we can draw a relationship between
 234 the quadrature conductivity and the surface conductivity σ_s^∞ as

$$235 \quad -\frac{\sigma''(\sqrt{f_1 f_2})}{\sigma_s^\infty} = \frac{M_n(f_1, f_2)}{\alpha \sigma_s^\infty} = \frac{R}{\alpha}. \quad (12)$$

236 Since R and α are both constants (independent of frequency, temperature, and saturation), this
 237 means that the quadrature conductivity and the surface conductivity are proportional to each
 238 other. Equations (10) to (12) are exact for the constant phase model, which is characterized by
 239 the absence of peaks in the quadrature conductivity spectra. They are good approximation for
 240 the Cole Cole model (Revil et al., 2017c).

241

242 **3. Materials and Methods**

243 Our dataset of is made up of a total of 69 experiments (labelled from E1 to E69). Each
 244 experiment corresponds to a distinct core sample. Experiments E1 to E44 and E49 to E52
 245 correspond to experiments made with crushed pellets sodium-MX80 bentonite and de-ionised
 246 water. The corresponding core samples are labelled MX80-Type I below. Experiments E45 to

247 E48 (MX80-Type I) are also made with the same crushed pellets sodium-MX80 bentonite
 248 saturated with saline solutions of known conductivities. Experiments E53 to E69 are made
 249 from a sodium-MX80 bentonite labelled GBM for highly compacted and granulated bentonite
 250 mixture (Garitte et al., 2015). The corresponding core samples are labelled MX80-Type II
 251 below.

252 Experiments E45 to E48 (between 90 – 100 % saturation) are used to calculate a
 253 formation factor (then a cementation exponent) and surface conductivity using pore water
 254 conductivities of 0.2, 1.0, 5.0, and 15 S m⁻¹ (NaCl, 25°C) (Table 1). The conductivities of the
 255 solutions used in making these samples were reached by mixing in NaCl with de-ionised water.
 256 The data from Table 1 are shown in Figure 4 and fitted with the linear conductivity model,
 257 which is valid above the so-called isoconductivity point (see Revil et al., 2017c).

258 The volumetric water content of each sample was determined using $\theta = m_w / (\rho_w V)$
 259 where m_w denotes the total mass of water (in kg) in the sample (hygroscopic and added), ρ_w
 260 is the mass density of water (in kg m⁻³) and V (m³) denotes the sample total volume (measured
 261 using a caliper). The gravimetric water content is defined as $w = m_w / m_s$ where m_s denotes the
 262 total mass of solid in the sample (in kg). The bulk and dry densities of the samples are then
 263 given by $\rho_b = m / V$ and $\rho_d = \rho_b / (1 + w)$, respectively, where $m = m_w + m_s$ and V denotes the
 264 total mass and total volume of the sample, respectively. The total volume of solids, voids and
 265 water in the sample are respectively given by $V_s = m_s / \rho_g$, $V_p = V - V_s$, and $V_w = m_w / \rho_w$
 266 where ρ_g is the grain density of bentonite (~2770 kg m⁻³). We have also the following
 267 definitions for the void ratio $e \equiv V_p / V_s$ (dimensionless), the connected porosity
 268 $\phi = V_p / V = e / (1 + e)$ (dimensionless), and the water saturation $s_w = V_w / V_p$ (dimensionless).
 269 The relationship between the volume water content θ and the gravimetric water content w is
 270 therefore obtained after few algebraic manipulations as $\theta = w(\rho_g / \rho_w) / (1 - \phi)$.

271 To determine the pore water conductivity of our samples, we mixed 20 g of MX80
272 powder (crushed pellets) with 500 ml of deionised water, placed the mixture under an agitator
273 for 48 hours and let it rest for 96 hours under room temperature and pressure. We then used a
274 conductivity meter and measured a solution conductivity of 0.0594 S m^{-1} at 25°C . If we account
275 for the dilution factor, the conductivity of the pore water is equal to 0.7 S m^{-1} at 25°C .
276 Nevertheless, if we plot the conductivity of the sample E28 with respect to the saturated core
277 samples saturated with NaCl solutions, we obtain a pore water conductivity of 2.5 S m^{-1} , much
278 higher than anticipated. Considering the surface conductivity σ_s in equation (2) of 0.26 S m^{-1} ,
279 ¹, our experiments are clearly above the isoconductivity point (Figure 2) and therefore the linear
280 relationships used in this paper are believed to be adequate (see Revil et al., 2017b).

281 Measurements of the cation exchange capacity (CEC) and specific surface area (SSA)
282 of the bentonite have been performed by various authors in the literature (see Bradbury and
283 Baeyens, 2002, Berger, 2008, Tang et al., 2008; and Karnland, 2010, for CEC, and Kiviranta
284 and Kumpulainen, 2011, and Gomez and Villar, 2010, for SSA). We obtain the following values
285 for the CEC and specific surface area of the MX-80 bentonite; $80 \text{ meq}/100\text{g}$, $31 \text{ m}^2\text{g}^{-1}$ (BET
286 method) and $573 \text{ m}^2\text{g}^{-1}$ (EGME “Ethylene Glycol Monoethyl Ether” method) (see Bradbury
287 and Baeyens, 2003; Bradbury et al., 2003; Molinero Guerra et al., 2017). In addition to this
288 information, we performed new measurements of the CEC of the two bentonites (Type I and
289 II) using cobaltihexamine method (see details in Guillaume 2002). We obtained a CEC of 81.9
290 $\pm 0.64 \text{ cmol}(+)/\text{kg}$ ($81.9 \text{ meq}/100 \text{ g}$) for the crushed pellets MX80 (Type I) and 87.2 ± 0.64
291 $\text{cmol}(+)/\text{kg}$ ($87.2 \text{ meq}/100 \text{ g}$) for GBM (Type II, 6 samples were used for replicates, 3 samples
292 per bentonite).

293 The mineralogy of the bentonite is dominated by Montmorillonite (between 70 and 90%
294 dry weight), with presence of Quartz, Feldspar, Muscovite and Calcite as well (Table 2). The
295 hygroscopic water contents of both bentonites were determined, using oven drying at 105°C

296 for a period of 120 hours, to be 6.07 (crushed pellets MX-80) and 8.64 for the GBM.

297 After mixing de-ionised water and bentonite powder in a mixing tray and using a spray,
298 the mixtures are placed in a metallic sample holder that was manufactured especially for this
299 purpose before being compressed using a uniaxial press (compression pressure depends on
300 desired compaction state). The resulting cylindrical samples are 5 cm in diameter with a height
301 generally comprised between 4 to 6 cm depending on the compaction state.

302 Complex conductivity spectra are obtained using a high-precision MFIA Impedance
303 Analyzer manufactured by Zurich Instruments (Figure 2). Measurements were taken
304 immediately after the creation of the samples to minimize the effect of drying (within minutes).
305 A radial configuration of electrodes is used (Jougnot et al., 2009). All electrodes are placed at
306 the centre height of the cylinder and at 90° from each other. Two current electrodes C1 and C2
307 impose the current and the potential electrodes P1 and P2 measure the potential at two points.
308 The potential and current electrodes are disposable pre-gelled Ag-AgCl electrodes used in the
309 medical industry (ECG). A geometrical factor is required to convert the impedance in terms of
310 complex conductivity. It depends on electrode geometry and was numerically determined using
311 COMSOL Multiphysics. We obtained values of 0.23 m and 0.25 m for sample heights of six
312 and eight centimetres, respectively.

313 Depending on the sampling rate and frequency range chosen, conducting frequency
314 sweeps on a sample takes a highly variable amount of time, ranging from 2-3 minutes for a
315 range of 1 Hz to 45 kHz and at 100 sample points all the way to over 12 hours for 1 mHz to 45
316 kHz. Due to the number of samples analysed, we decide to explore a reduced frequency range
317 comprised between 1 Hz and 45 kHz (Figure 3). We also conducted X-ray microtomography
318 tests and found that our samples were mostly homogeneous (Figure 1).

319

320 **4. Results**

321 4.1. Determination of the cementation exponent

322 From samples E45 through sample E48, a linear relationship was determined between
 323 the electrolyte (pore water) conductivity and in-phase conductivity of the core samples (Figure
 324 4). The (intrinsic) formation factor F was determined to be 14 (determined at a porosity of
 325 52%) and the surface conductivity $\sigma_s (s_w = 1) = \phi^{m-1} \rho_g B \text{CEC}$ was determined to be 0.26 S m^{-1}
 326 by fitting a linear function $\sigma' = \sigma_w / F + \sigma_s$ to the (in-phase) conductivity data obtained at the
 327 different salinities (Table 1 and Figure 4). Using Archie's law $F = \phi^{-m}$, the cementation
 328 exponent is determined to be $m=4.5$.

329

330 4.2. Prefactors

331 Both in-phase and quadrature conductivities can be related to the volumetric water
 332 content through power laws (Figures 5 and 6). The two power laws for the in-phase and
 333 quadrature conductivity can be written as

$$334 \quad \sigma' = \theta^m \sigma_w + \theta^p \Sigma_s, \quad (23)$$

$$335 \quad \sigma'' = \theta^p \frac{\Sigma_s R}{\alpha}, \quad (24)$$

$$336 \quad M_n = \theta^p R \Sigma_s, \quad (25)$$

337

338 where $\Sigma_s \equiv \rho_g B \text{CEC}$. Using $\rho_g = 2800 \text{ kg m}^{-3}$ (from crystallographic consideration regarding
 339 the crystalline framework of smectite), $B (\text{Na}^+, 25^\circ\text{C}) = 3.1 \times 10^{-9} \text{ m}^2 \text{s}^{-1} \text{V}^{-1}$ and a $\text{CEC} = 90$
 340 $\text{meq}/100 \text{ g} = 87 \times 10^3 \text{ C kg}^{-1}$ yields $\Sigma_s = 0.75 \text{ S m}^{-1}$. With $\alpha = 8$ and $R = 0.10$, the prefactor of
 341 the power law relationship for the quadrature conductivity is $a'' = \Sigma_s R / \alpha = 0.0095 \text{ S m}^{-1}$. If
 342 the in-phase conductivity is dominated by the surface conductivity, the prefactor of the power-
 343 laws relationship is $a' = \Sigma_s = 0.75 \text{ S m}^{-1}$. These slopes agree with the results shown in Figures
 344 5 and 6 for which a best fit yields $a' = \Sigma_s = 1.1 \pm 0.1 \text{ S m}^{-1}$ and $a'' = \Sigma_s R / \alpha = 0.0100 \pm 0.0004$

345 S m⁻¹.

346

347 **5. Discussion**

348 Figure 7 shows a plot of the normalized chargeability versus the conductivity of the
349 core samples. When surface conductivity dominates the conductivity response, the data should
350 stick only the slope given by $R = 0.10$. We see that this is not the case for the core samples used
351 in the present study indicating in turn that the pore water conductivity may be larger than used
352 in our estimate above. In Figure 8, we check that the normalized chargeability taken between
353 two frequencies is proportional to the quadrature conductivity at the geometrical mean of the
354 two frequencies with a slope close to the predicted slope.

355 Bentonite is composed essentially of smectite, which has the largest CEC among clay
356 minerals. In Figure 9, we plot the surface conductivity versus the reduced CEC (CEC divided
357 by the tortuosity defined as the product of the formation factor by the connected porosity). The
358 data of bentonite core samples used for the salinity experiment is plotted among a large dataset
359 from the literature. Bentonite has clearly a very large surface conductivity above all other core
360 samples because of its very high cation exchange capacity. In Figure 10, we plot the normalized
361 chargeability versus the surface conductivity. Again, the magnitude of both the normalized
362 chargeability and surface conductivity of bentonite is above those of other rock samples. The
363 inclusion of other porous materials in Figures 9 and 10 indicates that the dynamic Stern layer
364 model applied to induced polarization is very general.

365 Another way to plot the in-phase and quadrature conductivity is through the dependence
366 with the bulk and dry densities of the material. Indeed, the difference between the bulk density
367 and the dry density depends linearly on the volumetric water content. In Figure 11, we plot the
368 in-phase and quadrature conductivity versus the difference between the bulk and dry densities
369 (see data in Table 3). As expected, we observed linear relationships in a log-log scale.

370 Another point we want to address in this section is the applicability of the proposed
371 method to field conditions. The petrophysical investigations and results presented in this paper
372 can be applied to time-domain induced polarization data obtained in field conditions. For
373 instance, Abdulsamad et al. (2019) showed how induced polarization can be applied to estimate
374 the change in water content in an embankment associated with a leakage. Similarly, time-
375 domain induced polarization was recently applied to determine the transport properties of soil
376 for agriculture (Revil et al., 2017c; Revil et al., 2021) and to landslides (Revil et al., 2020)
377 using the dynamic Stern layer model of induced polarization described in the present
378 manuscript. Indeed, if we know the pore water conductivity, equations (7) and (9) are two
379 equations with two unknowns, the water content and the CEC. Tomography of time-domain
380 induced polarization data can be performed to obtain tomograms of the conductivity and
381 normalized chargeability. Then, we can apply these two equations to determine the water
382 content and CEC tomograms. The conductivity of the pore water can be obtained using a
383 speciation model accounting for the solubility of the minerals (see as an example for the
384 Collavo-Oxfordian formation, Leroy et al., 2007).

385

386

6. Conclusion

387 In deep geological repository concepts, compacted bentonite is a material considered
388 as a suitable barrier and an efficient buffer for radionuclides. We have performed complex
389 conductivity spectra of 69 core samples at different water content with different porosities
390 (compaction state) and saturation. The experiments have been mostly done at a low pore water
391 conductivity of 0.059 S m^{-1} at 25°C . The following conclusions have been reached:

392 (1) Both the in-phase conductivity and quadrature conductivity exhibit a power law
393 dependence with the (volumetric) water content.

394 (2) The prefactor coefficients for these power laws can be determined from the theory,

395 especially from the CEC of the bentonite alone.

396 (3) The values of the two power-law exponents $m = 4.5$ and $p = 3.1 \pm 0.1$ are consistent
397 with the expression $p = m - 1$.

398 Further works are needed to extend the present database to a broader salinity range.
399 Larger scale experiments in terms of time-lapse tomography of a large bentonite plug
400 undergoing desaturation would be welcome to see how time-lapse induced polarization
401 tomography can be used to assess the evolution of the water content in a bentonite-made
402 structure. Induced polarization appears a promising method to assess the monitor the
403 petrophysical characteristics of bentonites.

404

405 **Acknowledgements:** This work is funded by IRSN. We thank the two referees and the Editor
406 for fruitful comments that have helped us to shape a better version of our paper.

407

408 **References**

- 409 Abdulsamad F., A. Revil, A. Soueid Ahmed, A. Coperey, M. Karaoulis, S. Nicaise, and L.
410 Peyras, 2019, Induced polarization tomography applied to the detection and the monitoring
411 of leaks in embankments dams and dikes. *Engineering Geology*, **254**, 89–101.
412 <https://doi.org/10.1016/j.enggeo.2019.04.001>
- 413 Alawaji, H.A., 1999, Swelling and compressibility characteristics of sand–bentonite mixtures
414 inundated with liquids. *Appl. Clay Sci.*, **15** (3–4), 411-430.
- 415 Archie, G. E., 1942, The electrical resistivity log as an aid in determining some reservoir
416 characteristics. SPE-942054-G, **146**, 54–62. <https://doi.org/10.2118/942054-G>.
- 417 Berger, J., 2008, Hydration of swelling clay and bacteria interaction: An experimental in situ
418 reaction study, PhD Thesis, University Strasbourg 1.
- 419 Börner, F., 1992, Complex conductivity measurements of reservoir properties. *Advances in*
420 *Core Evaluation III (Reservoir Management)*: Gordon and Breach Science Publishers.
- 421 Bradbury, M. H, and B. Baeyens. 2003, Porewater Chemistry in Compacted Re-Saturated MX-
422 80 Bentonite, *Journal of Contaminant Hydrology*, 8th International Conference on
423 Chemistry and Migration Behaviour of Actinides and Fission Products in the Geosphere -
424 Migration 01, **61** (1): 329–38. [https://doi.org/10.1016/S0169-7722\(02\)00125-0](https://doi.org/10.1016/S0169-7722(02)00125-0).
- 425 Bradbury, M.H., Baeyens, B., 2002, Pore water chemistry in compacted re-saturated MX-80
426 bentonite: Physico-chemical characterisation and geochemical modelling (ISSN 1015–
427 2636). Switzerland.
- 428 Breede, K., Kemna, A., Esser, O., Zimmermann, E., Vereecken, H., Huisman, J. A., 2012,
429 Spectral induced polarization measurements on variably saturated sand-clay mixtures.
430 *Near Surface Geophysics*, **10** , 479–489. <https://doi.org/10.3997/1873-0604.2012048>.
- 431 Castellanos, E., Villar, M.V., Romero, E., Lloret, A., Gens, A. 2008. Chemical impact on the
432 hydro-mechanical behaviour of high-density FEBEX bentonite. *Phys. Chem. Earth*, **33**,

433 S516-S526

434 Chapman, N. A., 2006, Geological disposal of radioactive wastes-Concept, status and trends.

435 J. Iberian Geology, **32** (1), 7–14.

436 Chen, Y.-G., Cui, Y.-J., Tang, A. M., Wang, Q., Ye, W.-M., 2014, A Preliminary study on

437 hydraulic resistance of bentonite/host-rock seal interface. Géotechnique **64** (12), 997–

438 1002. <https://doi.org/10.1680/geot.13.p.209>.

439 Chen, Y.G., Zhu, C.M., Ye, W.M., Cui, Y.J., Wang, Q., 2015, Swelling pressure and hydraulic

440 conductivity of compacted GMZ01 bentonite under salinization–desalinization cycle

441 conditions. Applied Clay Science, **114**, 454-460.

442 Comparon, L., 2005, Etude expérimentale des propriétés électriques et diélectriques des

443 matériaux argileux consolidés (PHD thesis). Institut de Physique du Globe de Paris –

444 IPGP, 400 pp.

445 Cui, Y.J., Yahia-Aissa, M., Delage, P. 2002, A model for the volume change behavior of

446 heavily compacted swelling clays. Engineering Geology, **64**, 233-250.

447 Dias C.A., 2000, Developments in a model to describe low-frequency electrical polarization of

448 rocks. Geophysics, **65**, 437–451. <https://doi.org/10.1190/1.1444738>.

449 Dukhin S.S., Shilov V.N., 1974, Dielectrical phenomena and the double layer in disperse

450 systems and polyelectrolytes. Wiley, New York.

451 Garitte B., Weber, H.P., Müller, H.R., 2015, LUCOEX Deliverable D2.3 – Requirements,

452 manufacturing and QC of the buffer components. WP2 – Full-Scale Emplacement

453 Experiment (FE) at Mont Terri. EU report downloadable from www.lucoex.eu.

454 Gens, A., Alonso, E., 1992. A framework for the behaviour of unsaturated clay. Can. Geotech.

455 J., **29**, 1013-1032.

456 Guillaume, D., 2002, Etude expérimentale du système fer-smectite en présence de solution à

457 80 °C et 300° C. 207 pp., Doctoral dissertation, PhD. Thesis, Université de Nancy, France.

- 458 Ghorbani, A., Cosenza, P., Revil, A., Zamora, M., Schmutz, M., Florsch, N., and Jougnot, D.,
459 2009, Non-invasive monitoring of water content and textural changes in clay-rocks using
460 spectral induced polarization: A laboratory investigation. *Applied Clay Science*, **43**, 493–
461 502. <https://doi.org/10.1016/j.clay.2008>.
- 462 Gómez-Espina, R., and Villar, M.V., 2010, Geochemical and mineralogical changes in
463 compacted MX-80 bentonite submitted to heat and water gradients: *Applied Clay Science*,
464 **47**, 400–408. <https://doi.org/10.1016/j.clay.2009.12.004>.
- 465 Guo, G., Fall, M., 2021, Advances in modelling of hydro-mechanical processes in gas
466 migration within saturated bentonite: A state-of-art review: *Eng. Geol.*, **287**, 106123.
467 <https://doi.org/10.1016/j.enggeo.2021.106123>.
- 468 Herbert, H.J., Kasbohm, J., Sprenger, H., Fernandez, A.M., Reichelt, C., 2008, Swelling
469 pressures of MX-80 bentonite in solutions of different ionic strength. *Phys. Chem. Earth*,
470 **33**, S327-S342.
- 471 Hernandez, G.M., 2002, Etude expérimentale de la sorption d'eau et du gonflement des argiles
472 par microscopie électronique à balayage environnementale (ESEM) et analyse digitale
473 d'images. PhD Thesis, Université Louis Pasteur - Strasbourg I. [https://tel.archives-](https://tel.archives-ouvertes.fr/tel-00123521)
474 [ouvertes.fr/tel-00123521](https://tel.archives-ouvertes.fr/tel-00123521).
- 475 Jougnot D., Ghorbani A., Revil A., Leroy P., Cosenza P., 2010a, Spectral Induced Polarization
476 of partially saturated clay-rocks: A mechanistic approach: *Geophysical Journal*
477 *International*, **180**, 1, 210-224. <https://doi.org/10.1111/j.1365-246X.2009.04426.x>.
- 478 Jougnot, D., A. Revil, N. Lu, A. Wayllace, 2010b, Transport properties of the Callovo-
479 Oxfordian clay rock under partially saturated conditions. *Water Resources Research*, **46**,
480 8. <https://doi.org/10.1029/2009WR008552>.
- 481 Kanno, T., Wakamatsu, H., 1992, Water Uptake and Swelling Properties of Unsaturated
482 Bentonite Buffer Materials. *Can. Geotech. J.*, **29**, 1102–1107. <https://doi.org/10.1139/t92->

483 [127](#).

484 Karnland, O., S. Olsson, U. Nilsson. 2006, Mineralogy and sealing properties of various
485 bentonites and smectite-rich clay materials. ISSN 1404–0344. 43003619, Sweden.

486 Karnland, O., 2010, Chemical and mineralogical characterization of the bentonite buffer for
487 the acceptance control procedure in a KBS-3 repository.

488 Karnland, O., Muurinen, A., Karlsson, F., 2005, Bentonite swelling pressure in NaCl solutions
489 –Experimentally determined data and model calculations. E.E. Alonso, A. Ledesma (Eds.),
490 Advances in Understanding Engineered Clay Barriers: Proceedings of the International
491 Symposium on Large Scale Field Tests in Granite, Sitges, Barcelona, 12–14 November
492 2003, Taylor and Francis Group, London, 241-256.

493 Karnland, O., Olsson, S., Nilsson, U., Sellin, P., 2007. Experimentally determined swelling
494 pressures and geochemical interactions of compacted Wyoming bentonite with highly
495 alkaline solutions. Phys. Chem. Earth, 32 (1) (2007), pp. 275-286

496 Kemna A., Binley A., Cassiani G., Niederleithinger E., Revil A., Slater L., Williams K.H.,
497 Flores O.A., Haegel F.-H., Hördt A., Kruschwitz S., Leroux V., Titov K., Zimmermann
498 E., 2012, An overview of the spectral induced polarization method for near-surface
499 applications. Near Surf Geophysics, **10**, 453–468. [https://doi.org/10.3997/1873-](https://doi.org/10.3997/1873-0604.2012027)
500 [0604.2012027](https://doi.org/10.3997/1873-0604.2012027).

501 Kiviranta, L., Kumpulainen, S., 2011, Quality Control and Characterization of Bentonite
502 Materials.

503 Köhler, S., T., F., Müller, H., Gaus, I., 2015, Swiss backfilling concept – Requirements and
504 approaches for optimization of the bentonite barrier around SF/HLW disposal canisters.

505 Komine, N. Ogata, 1994, Experimental study on swelling characteristics of compacted
506 bentonite. Can. Geotech. J., **31**, 478-490.

- 507 Komine N., Komine H., Yasuhara K., Murakami S., 2009, Swelling characteristics of
508 bentonites in artificial seawater. *Can. Geotech. J.*, **46**, 2, 177-189.
- 509 Kruschwitz S., Yaramanci, U., 2004, Detection and characterization of the disturbed rock zone
510 in claystone with the complex resistivity method. *Journal of Applied Geophysics*, **57**, 63–
511 79. <https://doi.org/10.1016/j.jappgeo.2004.09.003>.
- 512 Kumpulainen, S., and L. Kiviranta. 2010. Mineralogical and Chemical Characterization of
513 various bentonite and Smectite-Rich Clay Materials Part A: Comparison and Development
514 of Mineralogical Characterization Methods Part B: Mineralogical and Chemical
515 Characterization of Clay Materials.” Finland, 43066642.
- 516 Leroy, P., Revil, A., 2009. A mechanistic model for the spectral induced polarization of clay
517 materials. *Journal of Geophysical Research: Solid Earth* **114**, B10202.
518 <https://doi.org/10.1029/2008JB006114>.
- 519 Leroy, P., Revil, A., 2004. A triple-layer model of the surface electrochemical properties of clay
520 minerals. *Journal of Colloid and Interface Science*, **270**, 371–380.
521 <https://doi.org/10.1016/j.jcis.2003.08.007>.
- 522 Leroy, P., A. Revil, S. Altmann, and C. Tournassat, 2007. Modeling the composition of the pore
523 water in a clay-rock geological formation (Callovo-Oxfordian, France). *Geochimica et*
524 *Cosmochimica Acta*, **71**(5), 1087-1097. <https://doi.org/10.1016/j.gca.2006.11.009>.
- 525 Madsen, F. T, 1998, Clay Mineralogical Investigations Related to Nuclear Waste Disposal.
526 *Clay Minerals* 33 (1): 109–29. <https://doi.org/10.1180/000985598545318>.
- 527 Martin, T. 2012, Complex resistivity measurements on oak, *European Journal of wood and*
528 *wood products*, **70**, 45-53, <https://doi.org/10.1007/s00107-010-0493-z>.
- 529 Martin, T., Nordsiek, S., Weller, A., 2015, Low-frequency impedance spectroscopy of wood,
530 *Journal of Research in Spectroscopy*, 910447.

- 531 Madsen, F. T., 1998, Clay Mineralogical investigations related to nuclear waste disposal: Clay
532 Minerals, **33** (1), 109–29. <https://doi.org/10.1180/000985598545318>.
- 533 Misra S., C. Torres-Verdín, A. Revil, J. Rasmus, and D. Homan, 2016, Interfacial polarization
534 of disseminated conductive minerals in absence of redox-active species. Part 1:
535 Mechanistic model and validation, Geophysics, **81**(2), E139-E157.
536 <https://doi.org/10.1190/GEO2015-0346.1>.
- 537 Mokni, N., Barnichon J.-D., Dick P., Son Nguyen T., 2016, Effect of technological macro voids
538 on the performance of compacted bentonite/sand seals for deep geological repositories.
539 International Journal of Rock Mechanics and Mining Sciences, **88**, 87-97, ISSN 1365-
540 1609. <https://doi.org/10.1016/j.ijrmms.2016.07.011>.
- 541 Molinero Guerra, A., N. Mokni, P. Delage, Y-J. Cui, A.M. Tang, P. Aimedieu, F. Bernier, and
542 M. Bornert, 2017, In-Depth characterisation of a mixture composed of powder/pellets
543 MX-80 Bentonite: Applied Clay Science, **135**, 538–
544 46. <https://doi.org/10.1016/j.clay.2016.10.030>.
- 545 Müller-Vonmoos, M., Kahr, G., 1983, Mineralogische Untersuchungen von Wyoming Bentonit
546 MX-80 und Montigel. Report. *Technischer Bericht NTB*. Vol. 83–12. ETH Zurich.
547 <https://www.research-collection.ethz.ch/handle/20.500.11850/114578>.
- 548 Norris, S., 2017. Radioactive waste confinement: clays in natural and engineered barriers –
549 introduction. Geological Society, London, Special Publications, **443**, 1–8.
550 <https://doi.org/10.1144/SP443.26>.
- 551 Ntarlagiannis D., Wu Y., Ustra A.T., 2019, Special issue: recent developments in induced
552 polarization, Near Surface Geophysics, **17**(6), 579.
- 553 Okay G., Cosenza P., Ghorbani A., Camerlynck C., Cabrera J., Florsch N., Revil A., 2013,
554 Characterization of macroscopic heterogeneities in clay-rocks using induced polarization:
555 Field tests at the experimental underground research laboratory of Tournemire (Aveyron,

- 556 France). *Geophysical Prospecting*, **61**, 134-152, <https://doi.org/10.1111/j.1365->
557 [2478.2012.01054.x](https://doi.org/10.1111/j.1365-2478.2012.01054.x).
- 558 Okay, G., Leroy, P., Ghorbani, A., Cosenza, P., Camerlynck, C., Cabrera, J., Florsch, N., Revil,
559 A., 2014. Spectral induced polarization of clay-sand mixtures: Experiments and modelling.
560 *Geophysics*, **79**, E353–E375. <https://doi.org/10.1190/geo2013-0347-1>.
- 561 Okko, O., Rautjaervi, J., 2006, Evaluation of monitoring methods available for safeguards use
562 at Olkiluoto geological repository Report on Task FIN C 1572 of the Finnish Support
563 Programme to IAEA Safeguards (ISBN 952-478-163–8). Finland.
- 564 Olhoeft, G.R., 1981, *Electrical Properties of Rocks*. Physical properties of rocks and minerals.
565 17 pp.
- 566 Pettersson, S., and Loennerberg, B., 2008, Final repository for spent nuclear fuel in granite -
567 the KBS-3V concept in Sweden and Finland. Presented at the Proceedings of the
568 international technical conference on the practical aspects of deep geological disposal of
569 radioactive waste, Ceske vysoke uceni technicke, Fakulta stavebni, Czech Republic, p.
570 346.
- 571 Revil, A., Atekwana E., Zhang C., Jardani A., and Smith S., 2012. A new model for the spectral
572 induced polarization signature of bacterial growth in porous media. *Water Resour. Res.*,
573 **48**, W09545. <https://doi.org/10.1029/2012WR011965>.
- 574 Revil, A., 2012, Spectral induced polarization of shaly sands: Influence of the electrical double
575 layer. *Water Resour. Res.* **48**. <https://doi.org/10.1029/2011WR011260>.
- 576 Revil, A., 2013a, On charge accumulations in heterogeneous porous materials under the
577 influence of an electrical field. *Geophysics*, **78**, 4, D271–D291.
578 <https://doi.org/10.1190/GEO2012-0503.1>.
- 579 Revil, A., 2013b, Effective conductivity and permittivity of unsaturated porous materials in the
580 frequency range 1 mHz–1GHz. *Water Resour. Res.*, **49**.

- 581 <https://doi.org/10.1029/2012WR012700>.
- 582 Revil A., Woodruff W.F., Torres-Verdín C., Prasad M., 2013a, Complex conductivity tensor of
583 hydrocarbon-bearing shales and mudrocks. *Geophysics*, **78**, no. 6, D403-D418.
584 <https://doi.org/10.1190/GEO2013-0100.1>.
- 585 Revil A., Eppehimer J.D., Skold M., Karaoulis M., Godinez L., Prasad M., 2013b, Low-
586 frequency complex conductivity of sandy and clayey materials. *Journal of Colloid and*
587 *Interface Science*, **398**, 193–209.
- 588 Revil, A., A. Binley, L. Mejus, and P. Kessouri, 2015, Predicting permeability from the
589 characteristic relaxation time and intrinsic formation factor of complex conductivity
590 spectra, *Water Resour. Res.*, **51**, 6672–6700. <https://doi.org/10.1002/2015WR017074>.
- 591 Revil, A., Coperey A., Shao Z., Florsch N., Fabricius I. L., Deng Y., Delsman J.R, Pauw P.S.,
592 Karaoulis M., de Louw P. G. B., van Baaren E. S., Dabekaussen W., Menkovic A., Gunnink
593 J. L., 2017c, Complex conductivity of soils: *Water Resour. Res.*, **53**, 8, 7121-7147.
594 <https://doi.org/10.1002/2017WR020655>.
- 595 Revil A., A. Soueid Ahmed, A. Coperey, L. Ravanel, R. Sharma, and N. Panwar, 2020. Induced
596 polarization as a tool to characterize shallow landslides, *Journal of Hydrology*, **589**,
597 125369. <https://doi.org/10.1016/j.jhydrol.2020.125369>.
- 598 Revil A., Schmutz M., Abdulsamad F., Balde A., Beck C., Ghorbani A. Hubbard S. S., 2021,
599 Field-scale estimation of soil properties from spectral induced polarization tomography,
600 *Geoderma*, **403**, 115380. <https://doi.org/10.1016/j.geoderma.2021.115380>.
- 601 Sauzeat, E., Guillaume, D., Neaman, A., Dubessy, J., François, M., Pfeiffert, C., Pelletier, M.,
602 Ruch, R., Barres, O., Yvon, J. Villéras, F., 2001 ; Caractérisation minéralogique,
603 cristallographique et texturale de l'argile MX-80. Rapport ANDRA No. CRP0ENG, pp.01-
604 001.

- 605 Schanz, T., Al-Badran, Y., 2014, Swelling pressure characteristics of compacted Chinese
606 Gaomiaozi bentonite GMZ01. *Soils Found.*, 54 (4), 748-759.
- 607 Schön, J., 1996, *Physical Properties of Rocks: Fundamentals and Principles of Petrophysics:*
608 Elsevier. <https://doi.org/10.1016/c2014-0-03002-x>.
- 609 Seigel, H., Nabighian, M., Parasnis, D.S. & Vozoff, K., 2007, The early history of the induced
610 polarization method: *The Leading Edge*, **26**, 3, 312-321.
- 611 Siddiqua, S., Blatz, J., Siemens, G., 2018, Evaluation of the impact of pore fluid chemistry on
612 the hydromechanical behaviour of clay-based sealing materials. *Can. Geotech. J.*, **48**, 2,
613 199-213.
- 614 Studds, P.G., Stewart, D.I., Cousens, T.W., 1998, The effects of salt solutions on the properties
615 of bentonite–sand mixtures. *Clay Miner.*, **33**, 651-660.
- 616 Sun, D., Zhang, L., Zhang B., Li J., 2015, Evaluation and prediction of the swelling pressures
617 of GMZ bentonites saturated with saline solution. *Appl. Clay Sci.*, **105**, 207-216.
- 618 Suzuki, S., Prayongphan, S., Ichikawa, Y., Chae, B., 2005. In situ observations of the swelling
619 of bentonite aggregates in NaCl solution. *Appl. Clay Sci.*, **29**, 89-98
- 620 Tang, A.-M., Y.-J. Cui, Le, T.-T., 2008, A Study on the thermal conductivity of compacted
621 bentonites. *Applied Clay Science*, **41**, 3, 181–189.
622 <https://doi.org/10.1016/j.clay.2007.11.001>.
- 623 Tartrat Y. T., Revil A., Abdulsamad F., Ghorbani A., Jougnot D., Coperey A., Yven B., de la
624 Vaissière R., 2019, Induced polarization response of porous media with metallic particles
625 – Part 10. Influence of desiccation. *Geophysics*. **84**, 5, A43-W32.
626 <https://doi.org/10.1190/geo2019-0048.1>.
- 627 Vaudelet P., A. Revil, M. Schmutz, M. Franceschi, P. Bégassat, 2012, Induced polarization
628 signature of the presence of copper in saturated sands. *Water Resources Research*, **47**,
629 W02526. <https://doi.org/10.1029/2010WR009310>.

- 630 Villar, M., 2005. MX-80 Bentonite. Thermo-Hydro-Mechanical Characterisation Performed at
631 CIEMAT in the Context of the Prototype Project, Informes Técnicos Ciemat.
- 632 Villar, M.V., Lloret, A., 2008. Influence of dry density and water content on the swelling of a compacted
633 bentonite. *Appl. Clay Sci.*, **39**, 38–49.
- 634 Vinegar, H.J. and Waxman M.H., 1984, Induced polarization of shaly sands. *Geophysics*, **49**,
635 1267-1287.
- 636 Volckaert, G., Sillen, X., Van Geet, M., Bernier, F., Mayor, J.C., Goebel, I., Bluemling, P.,
637 Frieg, B., and Su, K., 2004, Similarities and differences in the behaviour of plastic and
638 indurated clays. In Ruiz, P. Fernandez (Ed.). *Radioactive Waste Management - Community
639 Policy and Research Initiatives The sixth international conference on the management and
640 disposal of radioactive waste - Euradwaste '04*, (p. 955). France.
- 641 Waxman, M.H. and Smits, L.J.M., 1968, Electrical Conductivities in Oil-Bearing Shaly Sands:
642 *Society of Petroleum Engineers Journal*, **8**, 107-122. <http://dx.doi.org/10.2118/1863-A>.
- 643 Zhu, C.M., Ye, W.M., Chen, Y.G., Chen, B., Cui. Y.J., 2013, Influence of salt solutions on the
644 swelling pressure and hydraulic conductivity of compacted GMZ01 bentonite.
645 *Engineering Geology*, **166**, 74-80.
- 646

Tables

647
648
649
650
651
652
653
654

Table 1. Pore water conductivities (NaCl, 25°C) used in the calculation of the formation factor, cementation exponent and surface conductivity. The formation factor F and surface conductivity σ_s are determined from $\sigma_\infty = \sigma_w / F + \sigma_s$ the then Archie's law $F = \phi^{-m}$ is used to compute the power-law exponent m . The data given here correspond to saturated core samples.

ID	σ_w (S m ⁻¹)	σ' (S m ⁻¹)	ϕ (-)
E45	0.2	0.2835	0.553
E46	1.0	0.3161	0.544
E47	5.0	0.6111	0.526
E48	15	1.348	0.508
E28	0.0594 (*)	0.43789	0.519

655

(*) Using de-ionized water

656

657 **Table 2.** Mineralogy of Wyoming MX80 bentonite taken from various sources in the literature.
658 Mo., montmorillonite; Q, quartz; F, feldspar; M, muscovite; T, tridymite; C, calcite. We see that
659 montmorillonite is by far the most abundant component. The composition is given in Vol.%.

Source	Mo.	Q	F	M	T	C
Karland et al. (2006)	81.4	3	3.5	3.4	3.8	0.2
Madsen (1998)	75.5	15	5-8	< 1	-	-
Molinero Guerra (2018)	80	4	10	4	-	-
Kumpulainen and Kiviranta (2010)	81.7	3.8	1.5	5.3	2.6	0.5
Kiviranta and Kumpulainen (2011)	88.2	3.5	5.5	0.3	-	0.2
Mueller-Vonmoos and Kahr (1983)	75	15.2	5-8	< 1	-	0.7
Sauzeat et al. (2001)	> 80	5-6	4.5	2.8-3.8	-	0.3-1.4
Tang et al. (2008)	92	3	-	-	-	-
Villar (2004)	65-82	4-12	5-8	-	-	-
Montes Hernandez et al. (2007)	70.6	2.5	1.8	-	-	0.7

660

661

662 **Table 3.** Results of the experiments. ID described the experiment number. Θ denotes the water
 663 content. The quantities ρ_b and ρ_d denote the bulk density and the dry density, respectively. The
 664 quantity ϕ denotes the connected porosity. Finally the quantities s' and s'' denote the in-phase
 665 conductivity determined at the frequency of 345 Hz and M_n denotes the normalized
 666 chargeability taken as the difference in the in-phase conductivity between 10 Hz and 10 kHz.
 667 Experiments E45 to E48 (between 90 – 100 % saturation) are performed using pore water
 668 conductivities of 0.2, 1.0, 5.0, and 15 S m⁻¹ (NaCl, 25°C).

ID	Θ (-)	Sw (-)	ρ_b (g cm ⁻³)	ρ_d (g cm ⁻³)	ϕ (-)	σ' (S m ⁻¹)	σ'' (S m ⁻¹)	M_n (S m ⁻¹)
E1	0.174	0.465	1.91	1.73	0.374	0.03572	0.00042	0.00209
E3	0.155	0.344	1.68	1.52	0.450	0.00778	0.00008	0.00031
E4	0.159	0.371	1.74	1.58	0.429	0.01603	0.00019	0.00085
E5	0.185	0.545	2.02	1.83	0.339	0.04408	0.00055	0.00272
E6	0.209	0.417	1.59	1.38	0.501	0.03060	0.00009	0.00025
E7	0.222	0.464	1.67	1.45	0.478	0.05112	0.00019	0.00076
E8	0.25	0.617	1.9	1.65	0.405	0.06770	0.00023	0.00124
E9	0.234	0.525	1.77	1.54	0.445	0.10428	0.00049	0.00239
E10	0.274	0.541	1.64	1.37	0.506	0.04843	0.00009	
E11	0.298	0.619	1.73	1.44	0.482	0.09293	0.00019	
E12	0.311	0.703	1.85	1.54	0.443	0.18208	0.00043	0.00377
E13	0.344	0.897	2.05	1.71	0.384	0.26431	0.00056	0.00419
E14	0.368	0.661	1.59	1.23	0.557	0.15942	0.00034	
E15	0.396	0.751	1.71	1.31	0.527	0.19961	0.00044	0.00067
E16	0.417	0.821	1.78	1.36	0.507	0.24866	0.00065	0.00276
E17	0.42	0.842	1.81	1.39	0.499	0.26774	0.00051	0.00120
E18	0.424	0.858	1.82	1.40	0.494	0.26535	0.00063	0.00174
E19	0.427	0.868	1.83	1.41	0.492	0.24592	0.00049	
E20	0.429	0.878	1.85	1.42	0.488	0.27945	0.00064	0.00131
E21	0.435	0.899	1.86	1.43	0.484	0.28673	0.00082	0.00139
E22	0.338	0.536	1.36	1.03	0.630	0.07712	0.00019	
E23	0.408	0.645	1.43	1.02	0.632	0.20415	0.00111	0.00284
E24	0.457	0.779	1.6	1.14	0.587	0.22167	0.00086	0.00366
E25	0.5	0.900	1.73	1.23	0.556	0.33016	0.00156	0.00085
E26	0.513	0.956	1.8	1.28	0.537	0.29059	0.00110	0.00644
E27	0.516	0.96	1.8	1.28	0.538	0.36324	0.00124	0.00322
E28	0.536	1.033	1.87	1.33	0.519	0.43789	0.00204	0.00776
E29	0.539	1.045	1.88	1.34	0.516	0.39644	0.00203	0.00535
E30	0.544	1.067	1.9	1.36	0.510	0.42740	0.00175	0.00505
E31	0.456	0.677	1.36	0.91	0.673	0.13063	0.00080	0.00100
E32	0.564	0.945	1.68	1.12	0.597	0.33575	0.00209	0.00624
E33	0.417	0.554	1.1	0.68	0.753	0.13658	0.00115	0.00523
E34	0.484	0.68	1.28	0.8	0.712	0.18436	0.00153	0.00584
E35	0.546	0.809	1.44	0.9	0.675	0.23146	0.00180	0.00749
E36	0.592	0.914	1.57	0.97	0.648	0.30978	0.00264	0.01194
E37	0.597	0.931	1.59	0.99	0.642	0.33401	0.00231	0.00988
E38	0.661	1.096	1.76	1.1	0.603	0.32784	0.00230	0.00848
E39	0.536	0.738	1.29	0.76	0.727	0.17697	0.00171	0.00857
E40	0.686	1.057	1.66	0.97	0.649	0.44600	0.00361	0.01497
E41	0.485	0.621	1.09	0.61	0.782	0.18240	0.00197	0.00995
E42	0.606	0.834	1.36	0.76	0.727	0.31642	0.00374	0.01915
E43	0.708	1.036	1.58	0.88	0.683	0.41971	0.00363	0.01432
E44	0.701	0.936	1.39	0.7	0.749	0.32564	0.00399	0.01962
E45	0.498	0.90	1.73	1.09	0.553	0.283579	0.001621	0.007877
E46	0.506	0.93	1.77	1.09	0.545	0.316158	0.001881	0.008886

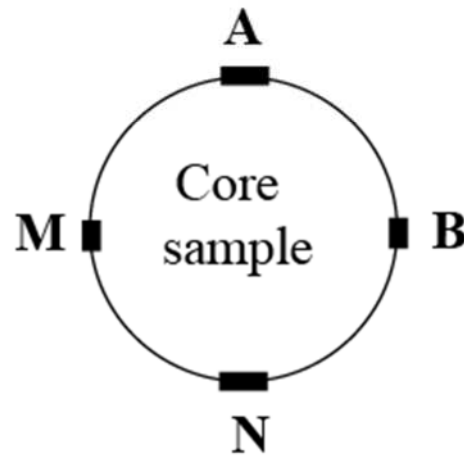
E47	0.527	1.003	1.84	1.31	0.526	0.61116	0.002642	0.010086
E48	0.552	1.087	1.91	1.36	0.508	1.348184	0.002354	0.008883
E49	0.528	1.003	1.84	1.31	0.526	0.29833	0.00140	0.00308
E50	0.516	0.962	1.8	1.28	0.537	0.34092	0.00172	0.00573
E51	0.303	0.667	1.81	1.51	0.455	0.11818	0.00020	
E52	0.645	1.05	1.71	1.07	0.614	0.42300	0.00341	0.01381
E53	0.636	0.959	1.57	0.93	0.663	0.25208	0.00168	0.00373
E54	0.673	1.046	1.66	0.99	0.644	0.36752	0.00243	0.00864
E55	0.381	0.697	1.64	1.26	0.547	0.15759	0.00046	
E56	0.324	0.528	1.39	1.07	0.615	0.06587	0.00015	
E57	0.460	1.015	1.97	1.52	0.453	0.30526	0.00095	
E58	0.454	0.989	1.95	1.50	0.460	0.27284	0.00073	
E59	0.420	0.840	1.80	1.39	0.500	0.16190	0.00037	
E60	0.715	1.023	1.55	0.83	0.699	0.39047	0.00244	
E61	0.729	1.052	1.58	0.85	0.693	0.33581	0.00248	0.00961
E62	0.705	1.002	1.52	0.82	0.703	0.36939	0.00302	
E63	0.463	0.736	1.49	1.03	0.630	0.13881	0.00056	
E64	0.538	0.945	1.73	1.19	0.570	0.22339	0.00086	
E65	0.515	0.875	1.65	1.14	0.588	0.22110	0.00099	
E66	0.559	1.011	1.80	1.24	0.553	0.33062	0.00161	
E67	0.239	0.566	1.84	1.60	0.423	0.02765	0.00013	
E68	0.691	1.090	1.70	1.01	0.634	0.38463	0.00241	0.00824
E69	0.691	1.094	1.71	1.02	0.632	0.32466	0.00203	0.00562

669

670

671

687

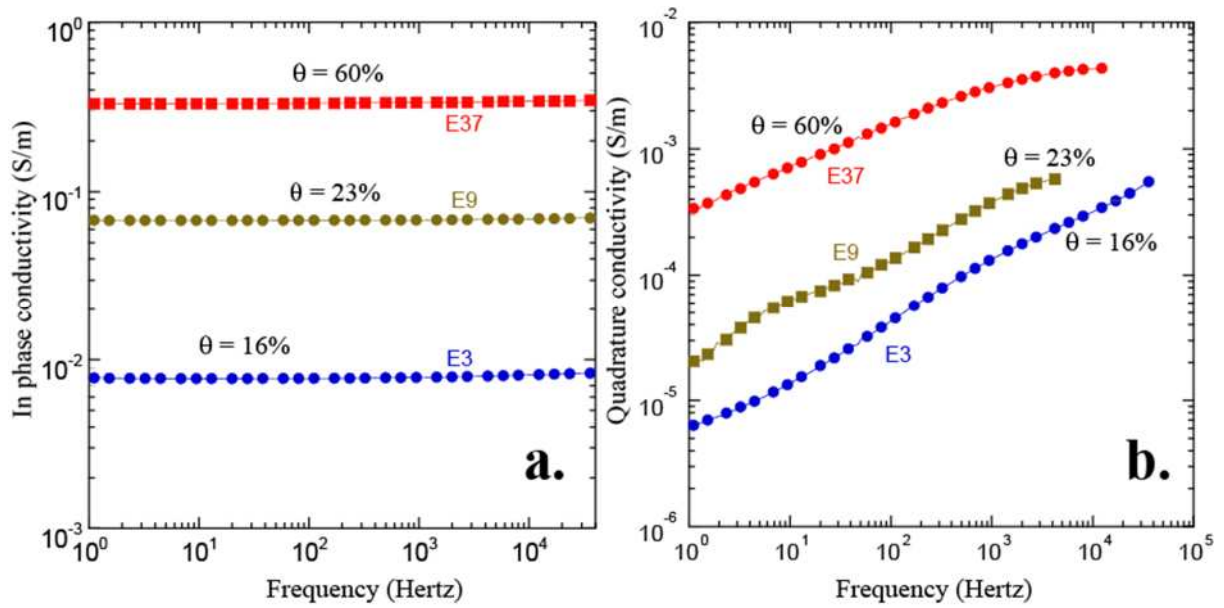
a. Impedance meter**b. Position of the electrodes**

688

689

690 **Figure 2.** Experimental setup. **a.** Impedance meter from Zurich Instrument used for the
691 complex conductivity measurements in the frequency range 1 Hz-45 kHz. **b.** Position of the
692 electrodes on the side of the core sample (A and B are current electrodes; M and N are potential
693 measurement electrodes).

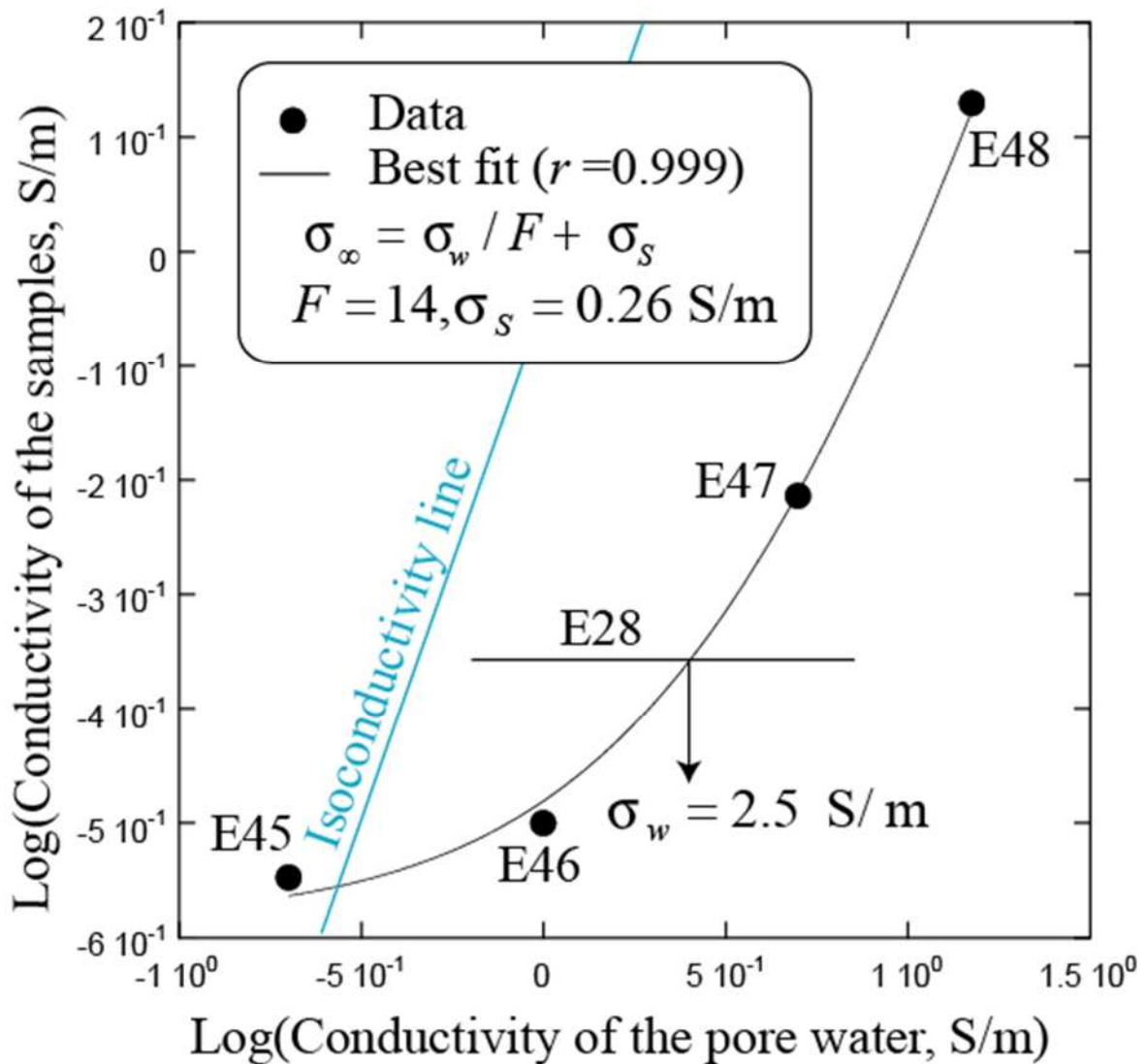
694



695
696

697 **Figure 3.** In-phase and quadrature conductivity spectra of three core samples characterized by
 698 distinct water contents (here expressed in Vol.%). **a.** In phase conductivity spectra. **b.**
 699 Quadrature conductivity spectra.
 700

701
702
703

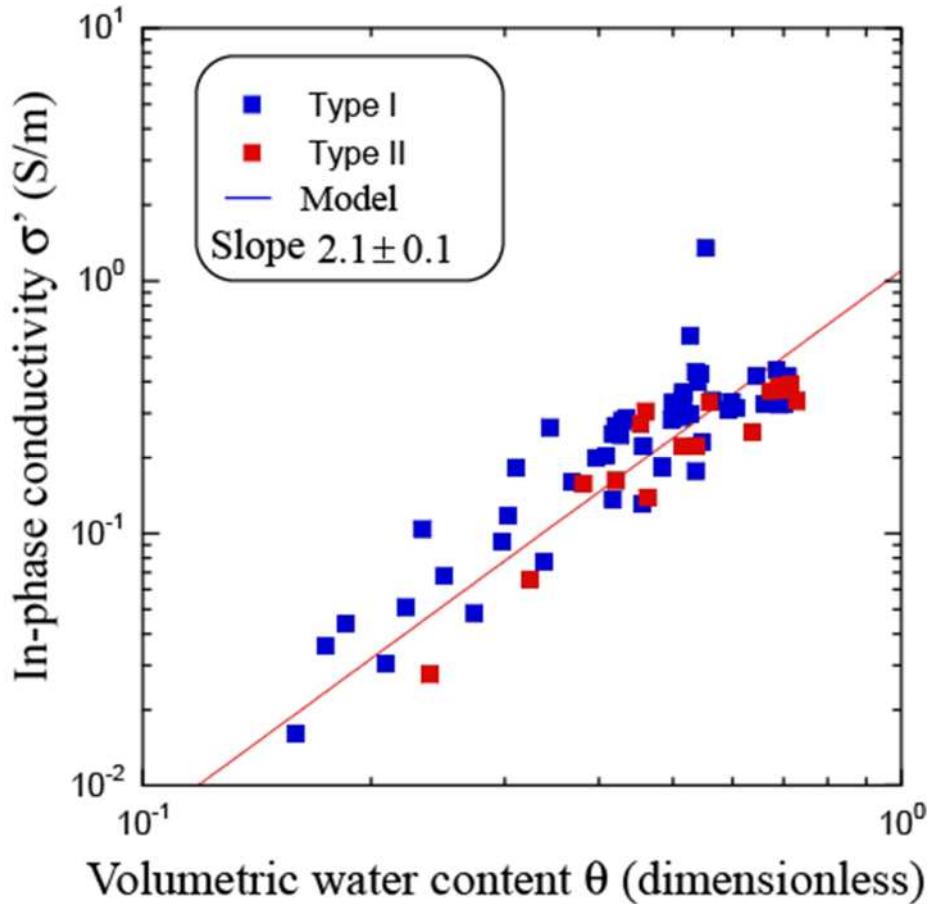


704
705

706 **Figure 4.** Conductivity of the saturated samples versus the conductivity of the pore water at
707 saturation and for a porosity of 0.53 ± 0.02 (data from Table 1). Sample E28 (also fully water-
708 saturated) is also saturated with distilled water. It is at the same porosity than the other core
709 sample (around 0.52). It indicates that the real conductivity of the pore water is around 2.5 S
710 m^{-1} (25°C). The value of the formation factor and the porosity (0.53 ± 0.02) yields a porosity
711 exponent $m = 4.5$. The isoconductivity line is the line for which the conductivity of the core
712 sample is equal to the conductivity of the pore water. This corresponds to the limit of the linear
713 (high salinity) conductivity model used in the main text.

714
715

716



717

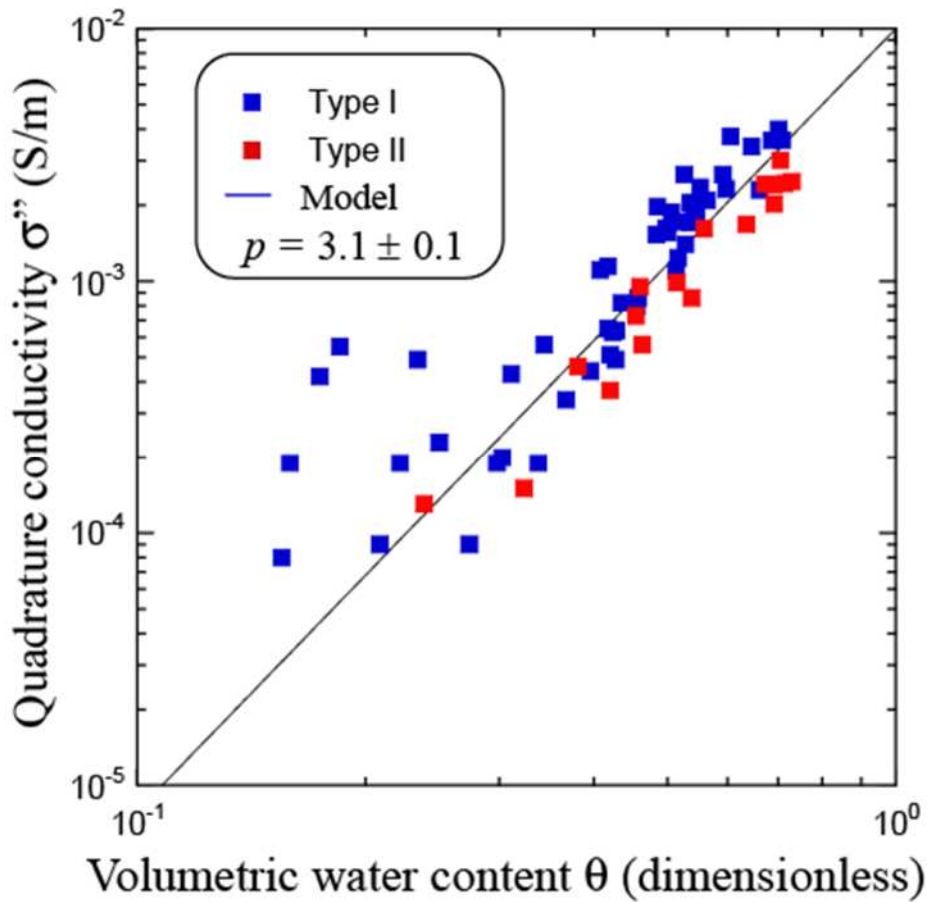
718

719

720 **Figure 5.** Dependence of the in-phase conductivity versus the water content ($r = 0.82$). The
 721 data are fitted with a power law function. The prefactor determined from the linear regression
 722 is equal to $1.1 \pm 0.1 \text{ S m}^{-1}$ close to the predicted value of $a' = \Sigma_s = 0.8 \text{ S m}^{-1}$. The slope determined
 723 from the best fit is equal to a power-law exponent of 2.1 ± 0.1 , much lower however than the
 724 cementation exponent determined from the porosity and formation factor ($m = 4.2$).

725

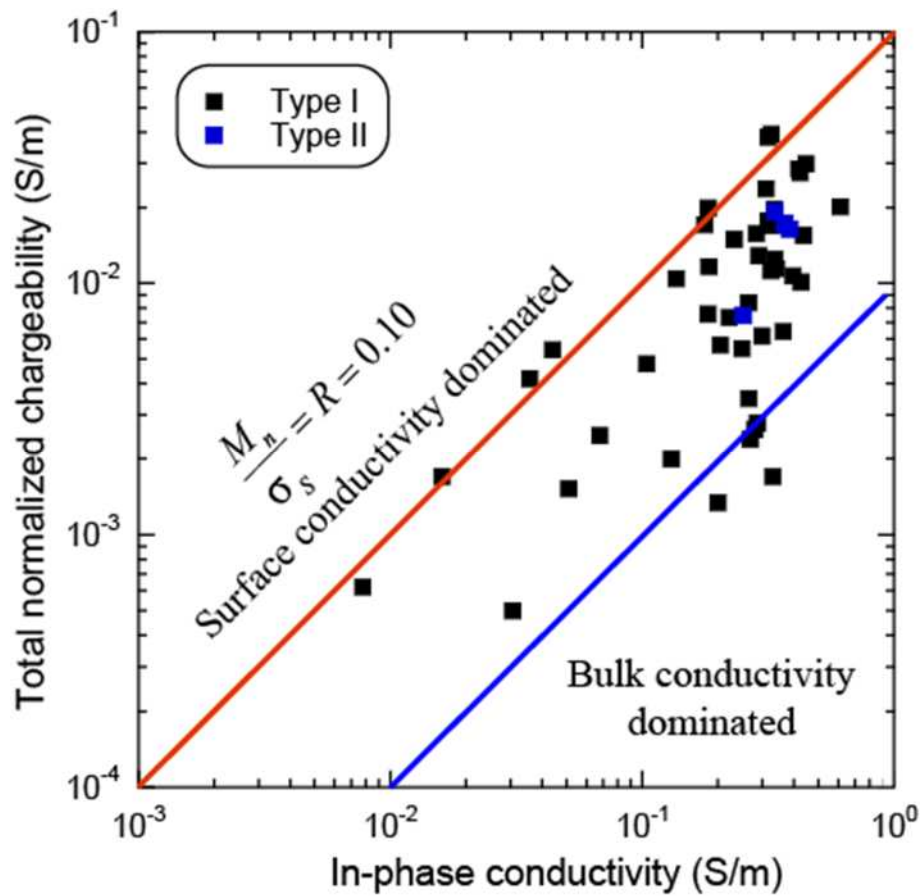
726
727
728



729
730

731 **Figure 6.** Dependence of the quadrature conductivity versus the water content ($r = 0.74$). The
732 data are fitted with a power-law function. The prefactor is equal to $0.0100 \pm 0.0004 \text{ S m}^{-1}$ close
733 to the theoretical prefactor determined in the main text and given by $a'' = \Sigma_s R/\alpha = 0.0095 \text{ S}$
734 m^{-1} . The porosity exponent is equal to $p = 3.1 \pm 0.1$ fairly consistent with the expression $p =$
735 $m - 1$ and $m = 4.5$ determined from the formation factor and the porosity (see Figure 4).
736

737
738



739
740
741
742
743
744
745
746
747
748
749
750

Figure 7. Normalized chargeability (twice the normalized chargeability determined from the difference in the conductivity between 1 Hz and 10 kHz) versus the in-phase conductivity. The plot shows that for some experiments, surface conductivity dominates the bulk conductivity and the data points are close to the red straight line. That said, there are experiments for which this is not the case and the data are close or below the blue line for which the bulk conductivity is ten times higher than the surface conductivity. These results are consistent with a high value of the pore water conductivity (2.5 S m^{-1} at 25°C).

751

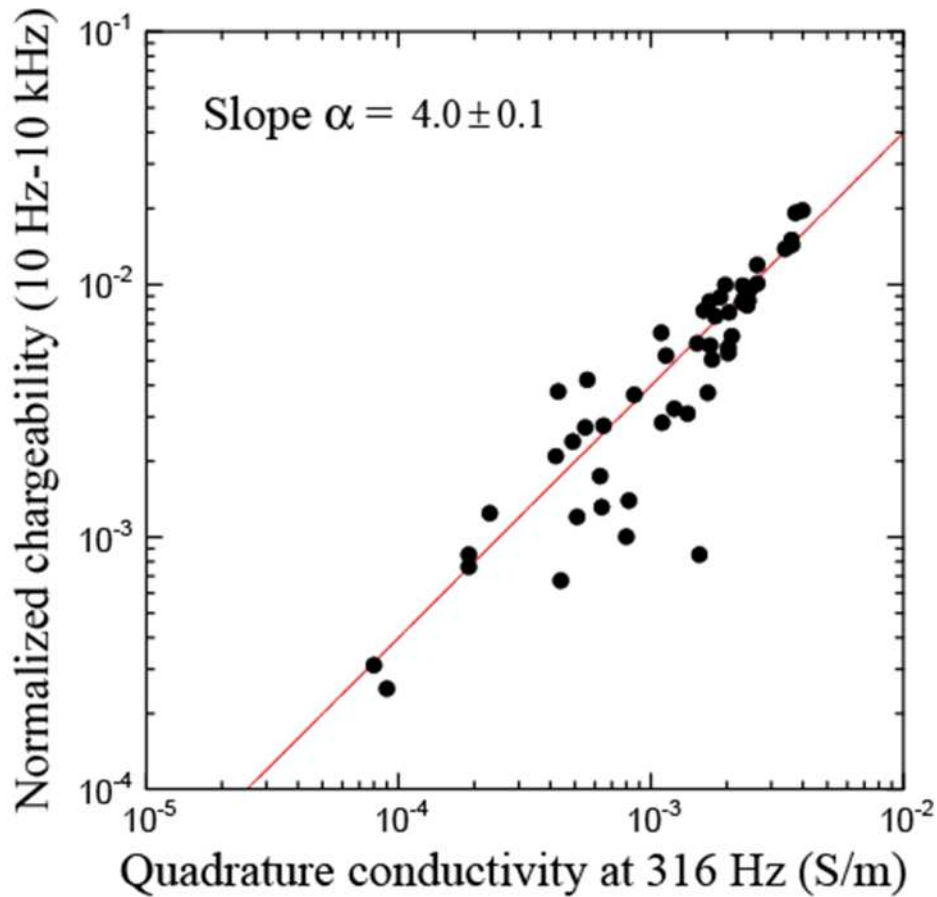
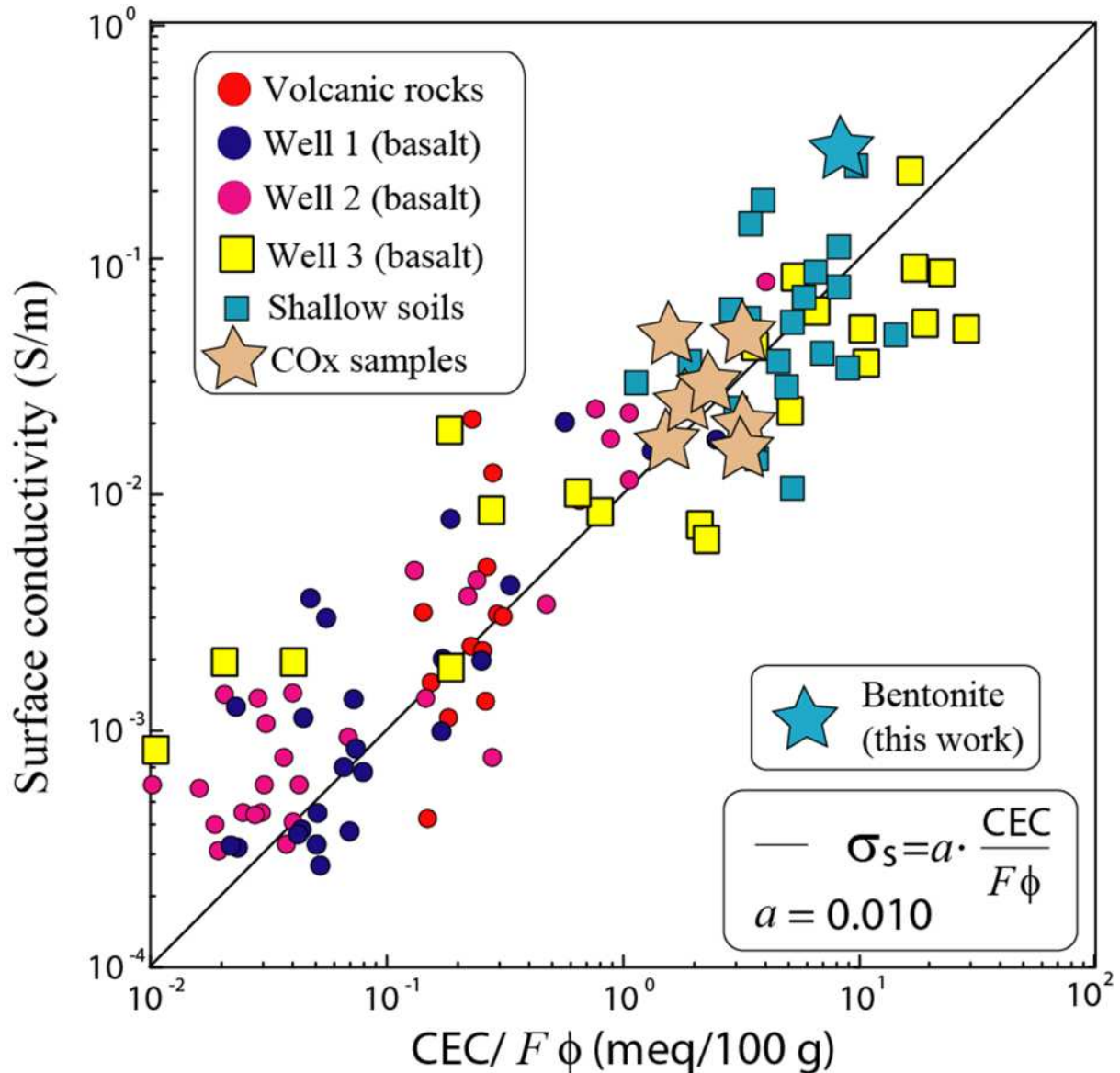
752
753
754

Figure 8. The normalized chargeability (taken here as the difference of the in-phase conductivity between 10 hertz and 10 kHz) versus the quadrature conductivity (at the geometric mean of the two frequency, 316 Hertz) for the core samples of Table 3 ($r = 0.69$). The predicted slope is given by $\alpha = -(2/\pi)\ln D \approx 4.4$ close to the one obtained through a linear regression ($\alpha = 4.0$). Consequently, the normalized chargeability obeys to the same dependence with the water content than the quadrature conductivity.

761
762
763
764

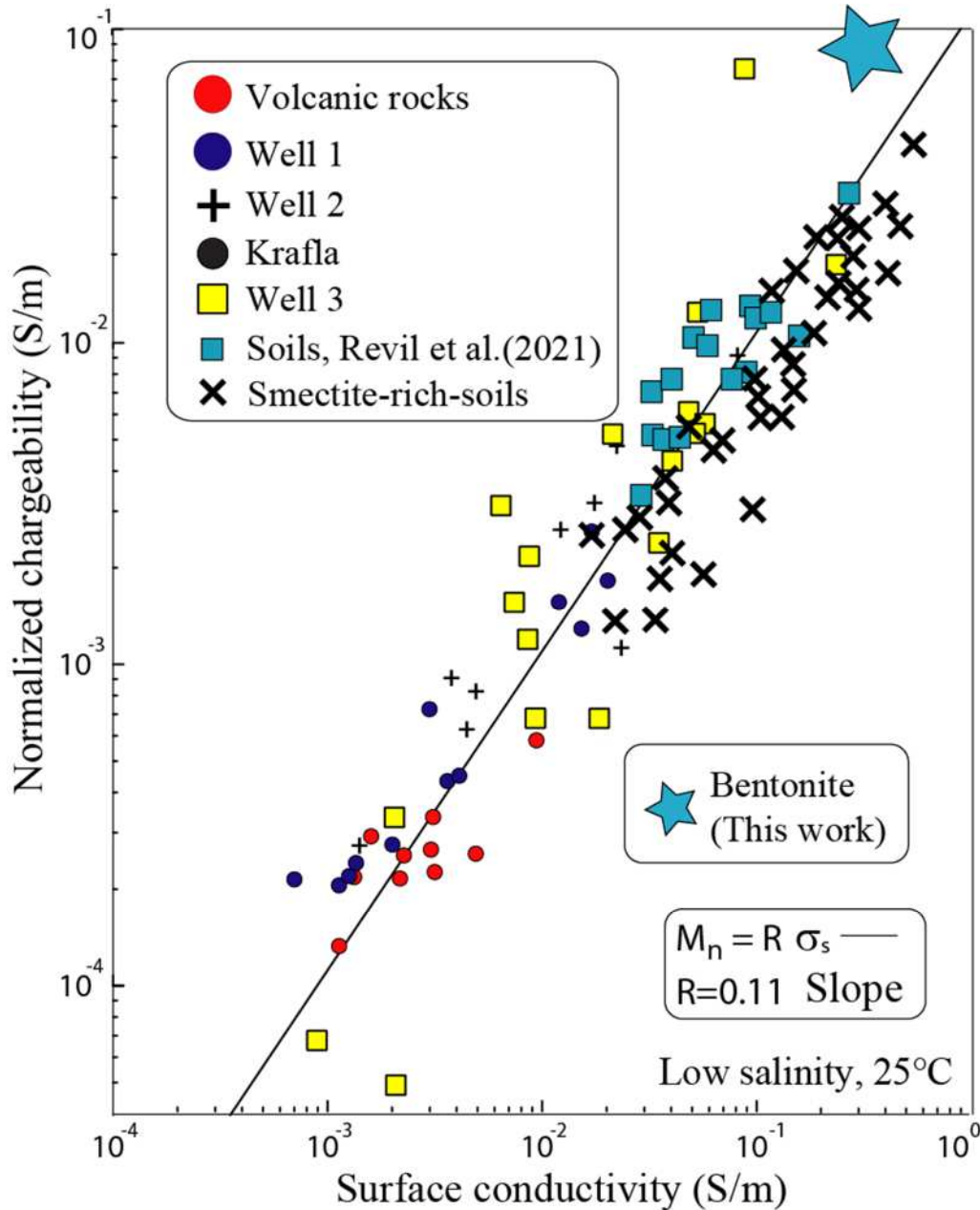
765



766
 767
 768
 769
 770
 771
 772
 773
 774

Figure 9. Surface conductivity versus the reduced CEC (CEC divided by the bulk tortuosity defined by the product of the formation factor and the connected porosity). COx stands for Callovo-Oxfordian clayrocks from the Paris Basin. The data on the volcanic rocks are from Revil et al. (2018), Ghorbani et al. (2018), and Revil et al. (2021b). The MX80 bentonite is characterized by the highest surface conductivity of the dataset ($r = 0.72$ for the dataset).

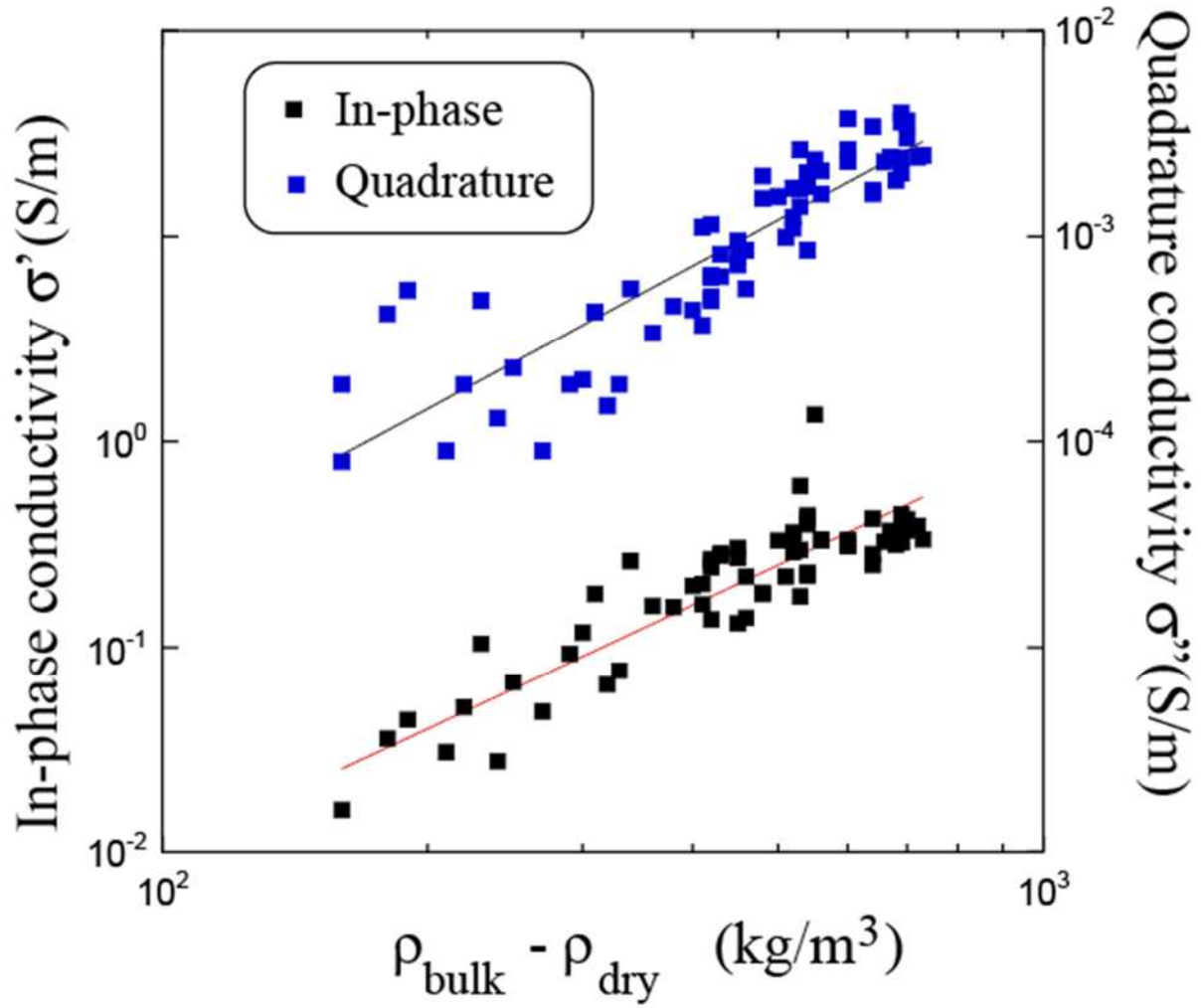
775



776

777 **Figure 10.** Relationship between normalized chargeability and surface conductivity.
 778 Comparison between the soil samples of the present study, the smectite-rich soil samples from
 779 the study of Revil et al. (2017) and volcanic rock samples (consolidated and not consolidated)
 780 from Hawaii and Krafla volcanoes (in Iceland, see Revil et al., 2018 and Ghorbani et al., 2018)
 781 excluding core samples with magnetite or pyrite. The slope of the trend provides the value of
 782 the fundamental dimensionless coefficient R , which is consistent with previous estimates of
 783 this parameter. Data from Revil et al. (2021b, volcanic rocks) and Revil et al. (2017, smectite-
 784 rich soils). For the MX80 bentonite, the surface conductivity is equal to $\sim 0.26 \text{ S m}^{-1}$ and the
 785 normalized chargeability is $\sim 0.01 \text{ S m}^{-1}$. The MX80 bentonite is characterized by the highest
 786 normalized chargeability of the entire dataset ($r = 0.83$ for the dataset).
 787

788



789

790

791 **Figure 11.** Relationship between the in-phase and quadrature conductivity versus the difference
 792 between the bulk and dry densities (correlation coefficient r of 0.60 and 0.86 respectively). .

793